Article

RBD-Modified Polyaniline-Based Label-Free Immunosensor for Sensitive Impedimetric Detection of Anti-SARS-CoV-2 Antibodies

Tea Romih [1], Nikola Tasić [1], Lea Bibič [1], Ajda Beltram [1], Ika Fazarinc [1], Mojca Benčina [2], Roman Jerala [2] and Samo B. Hočevar [1],*

[1] Department of Analytical Chemistry, National Institute of Chemistry, SI-1000 Ljubljana, Slovenia; tea.romih@ctk.uni-lj.si (T.R.); nikola.tasic@ki.si (N.T.); lea.bibic@universite-paris-saclay.fr (L.B.); ab9644@student.uni-lj.si (A.B.); if2912@student.uni-lj.si (I.F.)

[2] Department of Synthetic Biology and Immunology, National Institute of Chemistry, SI-1000 Ljubljana, Slovenia; mojca.bencina@ki.si (M.B.); roman.jerala@ki.si (R.J.)

* Correspondence: samo.hocevar@ki.si; Tel.: +386-1-4760-230

Abstract: The emergence of the SARS-CoV-2 virus and the associated pandemic has affected the entire human population. Human susceptibility to the virus has highlighted a tremendous need for affordable diagnostic systems to manage the pandemic and monitor the effectiveness of vaccination. We have developed a simple and label-free electrochemical immunosensor for the detection of human anti-SARS-CoV-2 IgG antibodies, which consists of a supporting screen-printed carbon electrode (SPCE) modified with an electrodeposited polyaniline film and glutaraldehyde, allowing effective immobilization of the SARS-CoV-2 spike glycoprotein receptor-binding domain (RBD) as a biorecognition element. The impedimetric immunosensor showed a linear response over a wide concentration range of 0.01–10 $\mu g\ mL^{-1}$, that is, 67 pM–6.7 nM, with a low detection limit of 25.9 pM. A dual working electrode configuration with a built-in negative control unit was demonstrated for practical field applications. The immunosensor was successfully used in a real serum sample from an infected patient and showed good reproducibility and fair agreement with ELISA. An optional amplification step with secondary goat anti-human IgG antibodies was demonstrated, resulting in an extended linear range and a detection limit as low as 0.93 pM.

Keywords: SARS-CoV-2; RBD; antibody detection; impedimetric immunosensor; built-in negative control unit

1. Introduction

The year 2020 will be remembered as the year of the COVID-19 pandemic caused by the SARS-CoV-2 virus. By now, the virus has already caused over 676 million infections and claimed nearly 6.8 million lives worldwide [1]. Three years later, it is more than evident that the pandemic has had a significant impact on public health, as well as on local and global economies [2].

Various molecular and serological methods are used to monitor viral infections. Currently, a real-time reverse transcription-polymerase chain reaction (RT-PCR) assay is at the forefront, also in combination with confirmatory chest scan tomography [3]. However, PCR-based methods require a thermocycling step, which somehow limits their practicality in point-of-care diagnostics. Van Elden et al. [4] also pointed out some disadvantages of the RT-PCR approach, such as contamination, duration, and sample handling. Isothermal amplification-based strategies such as RT-LAMP (reverse transcription loop-mediated isothermal amplification), CRISPR (clustered regularly interspaced short palindromic repeats), SHERLOCK (specific high-sensitivity enzymatic reporter unLOCKing), and others have been recognized as powerful alternatives [2,5–7]. These and related immunological approaches, for example, ELISA (enzyme-linked immunosorbent assay) and LFIA (lLateral flow immunoassay), are based on fluorescent and colorimetric detection and the use of

components such as fluorescent dyes, magnesium pyrophosphate, enzymes, antibodies, viral spike proteins, etc. [8,9].

It is known that SARS-CoV-2 viral load decreases significantly after the third week of infection, and at the same time, IgG load starts approaching its highest value [10]. Within this time frame, genosensing becomes less efficient, and immunosensors come to the fore; moreover, reliable antibody tests are essential for monitoring the long-term efficacy of vaccination. The current situation undoubtedly underscores the need for effective sensing systems that enable the transition from central laboratory analysis to on-site testing. In this regard, electrochemistry offers unique opportunities, as there are myriad geometries and sizes of supporting electrodes, numerous electrode materials, and virtually unlimited possibilities for their further modification. For example, electrochemical methods can be used for (i) detection of viral RNA by monitoring redox signaling probe activity, change in conductivity, or pH of the sample solution due to isothermal amplification processes such as RT-LAMP [11] and rolling circle amplification [12], (ii) detection of antigens [13], or (iii) detection of antibodies produced by the human immune system in response to viral infection [14].

Several reports of electrochemical sensors for the detection of SARS-CoV-2-specific antigens or antibodies have been published since late 2020, proliferating particularly since March 2021. The reported electrochemical detection principles are based on amperometry [15,16], voltammetry [13,17–19], potentiometry [19,20], impedance [14,21,22], and field-effect transistors [23]. Most sensors use biomolecules as biorecognition elements, but there are also reports on the use of molecularly-imprinted polymers [24]. Recent advances in electrochemical immunosensors for SARS-CoV-2 antigens and antibodies have been reviewed in detail by Ranjan et al. [25] and Mahshid et al. [26].

In this work, we present a sensitive and label-free impedimetric immunosensor for the detection of clinically relevant concentrations of human anti-SARS-CoV-2 antibodies with an integrated negative control unit. In addition to a relatively simple preparation protocol involving commercially available supporting SPCEs, without using precious metals and enzymes, we have demonstrated the excellent performance of the immunosensor and its favorable operation in a real sample from an infected patient.

2. Materials and Methods

2.1. Materials and Reagents

Hydrochloric acid (37%), NaCl, KCl, KH_2PO_4 (all Merck), aniline, glutaraldehyde (25%), $K_3[Fe(CN)_6]$, $K_4[Fe(CN)_6]$, NaN_3, glycine, IgG-free bovine serum albumin (BSA), human serum [cat. no. H4522] (all Sigma Aldrich), and $Na_2HPO_4 \cdot 2H_2O$ (VWR Chemicals) were of analytical grade. Aniline was freshly distilled before use, and all solutions used in this work were prepared with Milli-Q water (18.2 MΩ). $K_3[Fe(CN)_6]$ and $K_4[Fe(CN)_6]$ were diluted to 1.0 mM in 0.1 M KCl. Phosphate-buffered saline (PBS) was prepared according to the recipe of AAT Bioquest [27]. Glycine and BSA solutions were prepared in PBS, and 0.09% NaN_3 was added to BSA as a preservative. All solutions except HCl, $K_3[Fe(CN)_6]$, $K_4[Fe(CN)_6]$, and PBS were stored in a refrigerator at +2 °C.

Recombinant human coronavirus SARS-CoV-2 spike glycoprotein RBD (ab273065), recombinant human monoclonal anti-SARS-CoV-2 spike glycoprotein S1 antibodies [CR3022] (ab273073), unlabeled goat anti-human IgG antibodies (ab97161), and goat anti-human IgG antibodies conjugated to horseradish peroxidase (the latter used for the complementary ELISA assay, ab7153) were obtained from Abcam. After delivery, antibodies and other proteins were aliquoted in PBS and stored in test tubes with low protein binding at −20 °C until further use.

Human serum from a SARS-CoV-2-positive individual was obtained from the University Clinic of Respiratory and Allergic Diseases Golnik in Slovenia. The study "Identification of Neutralizing Antibodies Against SARS-CoV-2" was ethically approved by the Slovenian Medical Ethics Committee (No. 0120-333/2020/3, 14 September 2020).

2.2. Apparatus

Two types of supporting screen-printed carbon electrodes (SPCEs) were purchased from Metrohm DropSens: (i) DRP-C110 with a single carbon working electrode (circular, d = 4 mm); and (ii) DRP-X1110 with two carbon working electrodes (ellipsoidal, 4 mm width × 1.5 mm height). Both electrode systems had a carbon counter electrode and a silver quasi-reference electrode.

All electrochemical modifications and measurements were carried out using a Palm-Sens4 portable potentiostat/galvanostat (PalmSens BV) in combination with a cable connector for SPCEs (DRP-CAC 71606 or DRP-BICAC, Metrohm DropSens) or a MUX8-R2 multiplexer with two adapters for SPCEs (PalmSens BV). The instrument was controlled with PSTrace 5.8 software (PalmSens BV). All measurements were performed at room temperature (22–23 °C).

2.3. Preparation of the Immunosensor

2.3.1. Electrochemical Polymerization of Aniline

Prior to modification, the bare SPCEs were electrochemically tested by cycling the potential in the range of −1.0 to +1.0 V in a solution of 0.1 M KCl with 1.0 mM $[Fe(CN)_6]^{3-/4-}$ using a scan rate of 100 mV s^{-1}. Only the electrodes that showed comparable current responses were selected for further use. Freshly distilled aniline was diluted to 0.1 M in 0.5 M HCl, and the polyaniline film was electrochemically synthesized on the working electrodes of both types of SPCEs. The electrodes were immersed in 10 mL of the aniline solution and subjected to usually five cyclic voltammetric scans in a potential range of −0.2 V to +0.8 V at a scan rate of 100 mV s^{-1}. The polyaniline (PANI) coated electrodes were rinsed with deionized water and left overnight at ambient conditions before further modification.

2.3.2. Modification with Glutaraldehyde, Biorecognition Elements, and Glycine

The PANI-coated SPCEs were further modified with glutaraldehyde as a linker (2.5% in PBS, pH 7.4), then with either BSA (as a negative control unit, 10 μg mL^{-1} in PBS, pH 7.4) or RBD (as a biorecognition element, 10 μg mL^{-1} in PBS, pH 7.4), and finally with glycine (as a blocking agent, 1.0 M in PBS, pH 7.4) to block the unreacted glutaraldehyde moieties. Modifications were performed stepwise by drop-casting 10 μL of each solution onto the surface of a polyaniline-coated working electrode, followed by an incubation period in a humid atmosphere until the next modification step. The unbound reagents were thoroughly rinsed from the electrode surface with deionized water and PBS. The detailed procedure is shown in Scheme S1.

2.4. Impedimetric Immunosensing

The immunosensor was first exposed to a 10 μL sample of human anti-SARS-CoV-2 IgG antibodies for one hour, followed by rinsing and (optionally) by exposure to 10 μL of unlabeled goat anti-human IgG secondary antibodies (the latter usually at a concentration of 25 μg mL^{-1}) for signal amplification. The analytical performance of the immunosensor was investigated in the concentration range of 0.01–10 μg mL^{-1} by electrochemical impedance spectroscopy (EIS) in the presence of 1.0 mM $[Fe(CN)_6]^{3-/4-}$ in 0.1 M KCl. All measurements were performed at the formal potential of the $Fe(CN)_6^{3-/4-}$ redox probe (E_{dc} = +0.14 V) with an AC potential amplitude of 20 mV and 30 measurement points in the frequency range of 10 kHz to 100 mHz. The complementary ELISA protocol is described in the Supplementary Material.

3. Results and Discussion

The immunosensor architecture comprised the RBD subunits of the SARS-CoV-2 spike glycoprotein bound to a pre-modified SPCE surface to efficiently bind target antibodies, that is, human anti-SARS-CoV-2 IgGs. Optionally, unlabeled secondary antibodies, in this case, goat anti-human IgGs, were added to bind with the primary antibodies and increase the sensitivity of the electrochemical immunosensor, as schematically shown in

the graphical abstract. Incubation times similar to those used in the ELISA assay were used, while binding of the antibodies was detected by the increase in charge-transfer resistance (R_{ct}) obtained from impedimetric measurements in the presence of the redox probe $Fe(CN)_6^{3-/4-}$. Immunosensors were used as disposable devices for one-shot analysis.

3.1. Synthesis of PANI Film

PANI can be used as a suitable modifier that enables the effective immobilization of biomolecules through covalent bonding [28,29]. In conjunction with glutaraldehyde, the latter is expected to form bridges between primary and secondary amine groups in the PANI chain and with various functional groups on the protein surface through (predominantly) imine and enamine bonds [30]. Some researchers propose instead that the proteins bind to glutaraldehyde, which spontaneously polymerizes within the PANI network, whereas PANI and glutaraldehyde do not react [31]. Nevertheless, we found that a combination of PANI and glutaraldehyde allowed consistent immobilization of proteins on the SPCE surface, being stable and not easily washed away. This is particularly convenient for immunosensors, which need to be thoroughly rinsed after the incubation step(s) to limit non-specific binding and avoid false-positive results.

Therefore, the initial study focused on obtaining an electrochemically reproducible PANI layer with a favorable low resistance. During the electrochemical deposition of the PANI film, it was determined that the number of voltammetric scans must be low to achieve optimal sensing performance (as a support for further modifications), with five cycles being the optimum. The first five typical cyclic voltammograms during the deposition of PANI film on the supporting SPCE are shown in Figure 1a, indicating a successive increase in the current signal as a result of the growth of the PANI film. As can be seen in Figure 1b, the increase in polymerization cycles also led to a significant increase in the square-wave voltammetric response of the PANI-modified electrodes in the presence of $Fe(CN)_6^{3-/4-}$. Moreover, with the increasing number of electrochemical polymerization cycles, the formation of an additional signal at more positive potentials corresponding to the oxidation of leucoemeraldine to emeraldine salt was observed. Since this signal is relatively close to the signal of the $Fe(CN)_6^{3-/4-}$ redox probe at about +0.2 V, it can be a major obstacle for further electrochemical detection. Therefore, a protocol with only five cyclic voltammetric scans at 100 mV s^{-1} in a potential range of −0.2 V to +0.8 V was used to construct the first modification layer, which also resulted in satisfactorily low background noise.

The PANI-modified SPCEs were also characterized by EIS, and the corresponding results are presented in Figure 1c. The spectra obtained for the bare SPCE and the electrodes modified with one or two electrodeposition cycles show both the large semicircle, and the diffusion tail, which can be easily fitted with the Randles equivalent circuit (see Figure 1d), where R_S corresponds to the resistance of the solution, R_{ct} is the charge-transfer resistance associated with the redox species, W is the Warburg constant phase element modeling the diffusion, and Q is the constant phase element describing the non-ideal double-layer capacitance. Impedimetric response for the PANI-modified electrodes, characterized by a still considerable charge-transfer resistance but lower than that of the bare SPCE, is probably due to the porosity of the thin PANI film formed on the electrode surface after one and two electrodeposition cycles. As the number of polymerization cycles increased, the surface of the electrode became densely covered with the conductive PANI film, and the impedimetric behavior was apparently dominated by diffusion. In contrast to one or two electrodeposition cycles, the obtained data for five and more electrodeposition cycles should be fitted with simplified circuits, that is, a very good statistical agreement ($\chi^2 \approx 10^{-3}$) was obtained with the equivalent circuit R_S-W, in which the solution resistance is characterized by R_S, whereas the diffusion is modeled by Warburg (W), which is, in fact, a constant phase element (Q) with a phase angle (φ) of 45° and a fixed n parameter of 0.5 (Figure 1d). It appears that the reason for a well-developed voltammetric response after five electrodeposition cycles, as shown in Figure 1b, and a relatively low charge-transfer

resistance, as shown in Figure 1c, was a uniform growth of a dense and conducting PANI layer defined by a semi-infinite diffusion of redox species. In addition, the thicknesses of the electrodeposited PANI layers (h) were calculated using the following equation [32]:

$$h = \frac{qM}{\rho AnF} \tag{1}$$

where q stands for the electrodeposition charge extracted from the cyclic voltammetric polymerization curves, M is the molecular weight of aniline (93.13 g mol^{-1}), A represents the geometric area of the working electrode (0.1256 cm^2), n is the number of electrons involved in the polymerization reaction ($n = 2$), ρ is the density of PANI (1.33 g cm^{-3} [33]), and F is Faraday constant (96485 C mol^{-1}). Accordingly, the calculated thicknesses were 55 nm, 107 nm, 358 nm, 1.41 μm, 3.63 μm, and 27.1 μm for 1, 2, 5, 10, 15, and 25 electrodeposition cycles, respectively. These results are consistent with the electrochemical studies shown in Figure 1b,c and demonstrate that the increased number of electrodeposition cycles leads to the formation of denser and thicker structures characterized by diffusion-controlled EIS spectra (Figure 1c), along with a relatively high square-wave voltammetric response for $Fe(CN)_6^{3-/4-}$ (Figure 1b). The corresponding plots of thickness versus electrodeposition cycles/time are shown in Figure S1.
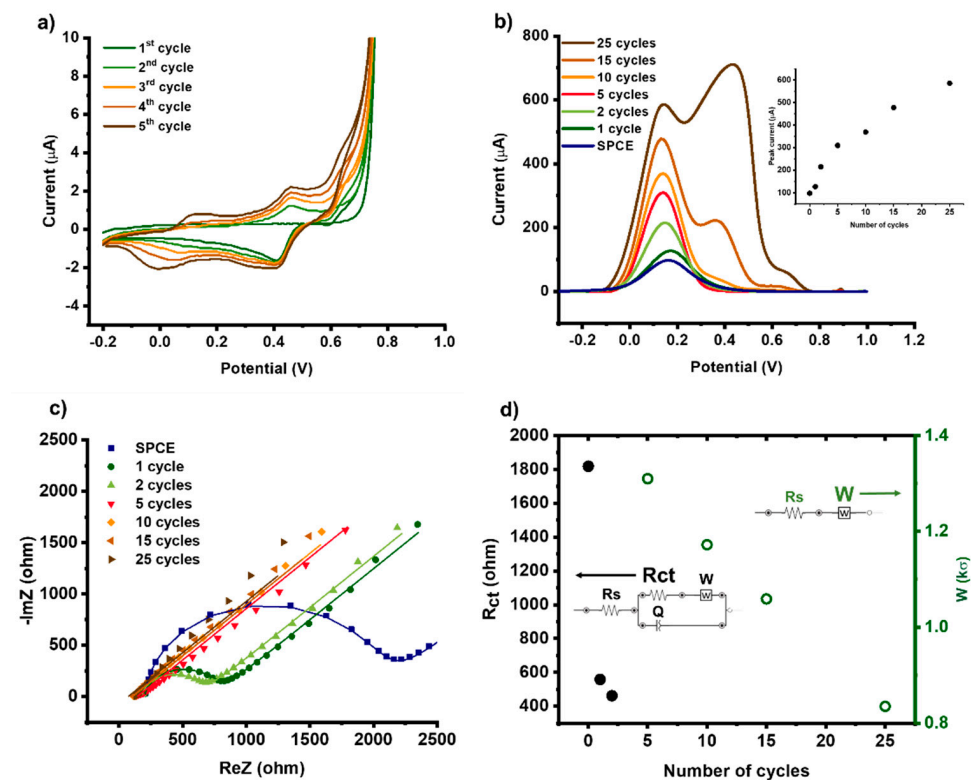

Figure 1. Five cyclic voltammograms (CVs) during electrodeposition of PANI recorded in 0.5 M HCl with 0.1 M aniline (**a**). Square-wave voltammograms (**b**) and electrochemical impedance spectra (EIS: symbols for measurements, lines for fitted data) (**c**) recorded in 0.1 M KCl with 1.0 mM [Fe(CN)$_6$]$^{3-/4-}$ using SPCEs modified with a different number of PANI electrodeposition cycles. Decrease in charge-transfer resistance (R_{ct}) for zero, one, and two cycles of PANI electrodeposition (black symbols, left Y axis) obtained by fitting raw impedance data using the Randles circuit (inset), and the decrease in Warburg constant phase element (W) for a higher number of PANI electrodeposition cycles (white-green symbols, right Y axis) obtained by fitting raw impedance data using the simpler equivalent circuit, i.e., R_s-W (inset) (**d**).

3.2. Glutaraldehyde Crosslinking

The initial experiments have shown that further modification of the electrodeposited PANI film with glutaraldehyde is rather challenging. Glutaraldehyde exists in a solution as a complex mixture of various forms, that is, from monomers, linear and cyclic oligomers to higher polymers, depending on factors such as pH, concentration, and temperature. Modification procedures using glutaraldehyde should, therefore, be developed empirically and tailored to each individual protein [34]. It is also important that glutaraldehyde solutions are always prepared freshly before use and that further modifications with proteins are performed immediately after the short rinsing sequence; otherwise, the crosslinking is insufficient due to the instability of glutaraldehyde.

After optimization, the modification protocol that proved the most suitable within the current immunosensor architecture included fresh 2.5% glutaraldehyde solution in a PBS buffer (pH 7.4) for effective immobilization of RBD (as a positive control unit) or BSA (as a negative control unit). Both protein layers (RBD or BSA) had to be further incubated with 1.0 M glycine in PBS to block unreacted aldehyde groups.

Stepwise modification of the supporting electrode was monitored by EIS, and the corresponding data are presented in Figure 2.
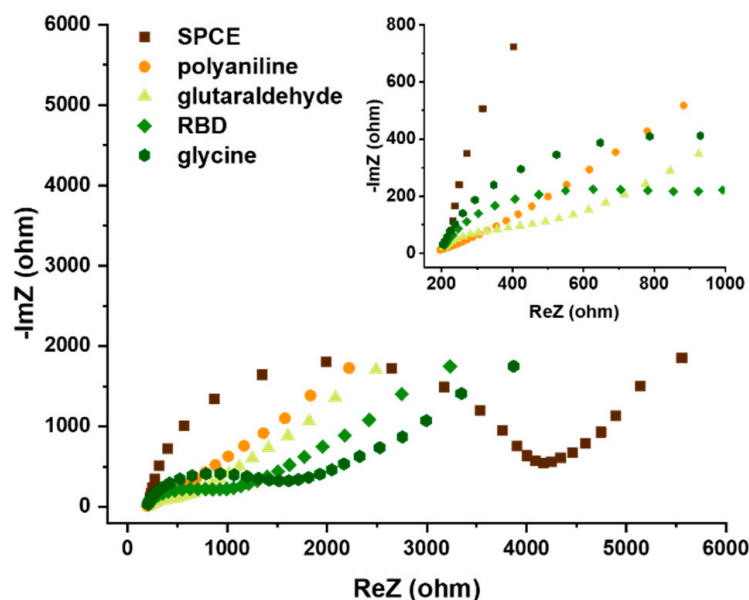

Figure 2. EIS (Nyquist plots) measurements for a stepwise preparation of the immunosensor monitored in 0.1 M KCl with 1.0 mM $[Fe(CN)_6]^{3-/4-}$ as the redox probe. The high-frequency range for all recorded spectra is shown in the inset.

It can be observed that the modification of rather resistive SPCE (R_{ct} = 3654 ohms) with the conductive PANI considerably affected the shape of the impedance spectrum, exhibiting only the contributions of solution resistance and diffusion, as discussed in the previous section. The subsequent incorporation of glutaraldehyde was characterized by the appearance of a semicircle, indicating that a resistive layer was formed on the PANI film. In the next step, crosslinking between PANI and RBD revealed a further increase in impedance compared to the previous modification step. It is known that the interior of RBD is positively charged, while its surface, which typically targets host cell ACE2 receptors, is predominantly negatively charged [35,36]. This suggests that the increased impedimetric signal in the measurements with a negatively charged $[Fe(CN)_6]^{3-/4-}$ redox probe after modification with RBD could be a solid indicator of successful RBD binding to the modified electrode surface via its positively charged fragment. Finally, modification with glycine, aimed at preventing non-specific binding during incubation, resulted in a further increase in impedance.

3.3. Electroanalytical Performance

After optimizing the modification protocol, we studied the electroanalytical performance of the immunosensor using an impedimetric approach. The sensor was tested over a wide concentration range of 0.01–10 µg mL^{-1}, that is, 67 pM–67 nM, and analytical signals were obtained from the raw spectra shown in Figure 3. Data were fitted using the modified Randles circuit R_S-($R_{ct}W \mid\mid CPE_{dl}$), where R_S stands for the solution resistance, R_{ct} corresponds to the charge-transfer resistance within the sensor interface, the Warburg element (W) represents the diffusion of redox species in solution, and CPE_{dl} denotes a non-ideal double layer capacitance. The difference in charge transfer resistance of the incubated sensor with and without target antibodies (ΔR_{ct}) was used as the analytical signal, and the corresponding calibration plot is depicted in the inset of Figure 3 involving error bars calculated as standard errors of four measurements carried out with four identically prepared immunosensors per each data point.
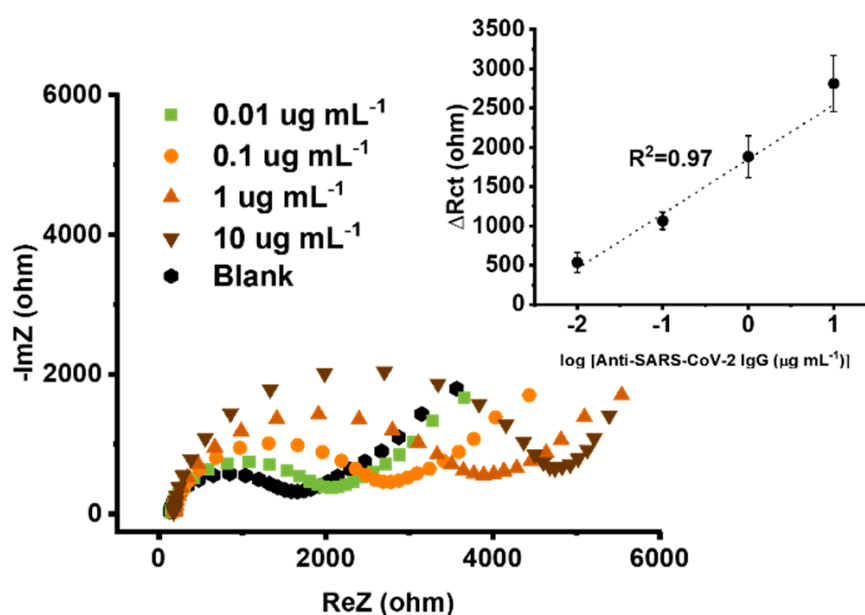

Figure 3. EIS (Nyquist plots) for different concentrations of anti-SARS-CoV-2 IgGs and the corresponding calibration plot in the inset (n = 4).

A linear impedimetric response of ΔR_{ct} vs. log[Anti-SARS-CoV-2 IgG] was obtained ($r^2 = 0.97$), along with a very low detection limit of 25.9 pM. The detection limit was calculated using the 3σ criterion for measuring with four identically prepared sensors for each data point. In addition, the sensor-to-sensor reproducibility was tested yielding the value of ca. 10% for 0.1 µg mL^{-1} data point. A somewhat higher value is primarily due to the known intrinsically lower reproducibility of commercially supported screen-printed electrodes.

3.4. Practical Application with Dual Electrode

A built-in negative control unit in the sensing system is advantageous from the practical application perspective, as is the case in, for example, lateral flow assay strips. For this purpose, we employed a supporting dual SPCE, that is, involving two integrated carbon electrodes that can be modified individually. After the electrodeposition of PANI and modification with glutaraldehyde, we modified one working electrode with BSA (negative control unit) and the other one with RBD (positive control unit). During the immunoassay, we incubated both electrodes with the same concentration of human anti-SARS-CoV-2 IgGs. As shown in Figure 4, the immunosensor revealed very well-defined signals and clearly differentiated between positive and negative controls. It should be noted here that the stepwise preparation was performed with smaller volumes of the modification

solutions, that is, instead of 10 μL, as in conventional SPCE, only 6 μL was used due to differences in the electrode geometry and size. Consequently, the absolute values of the impedance and their relative changes were affected by this peculiarity.
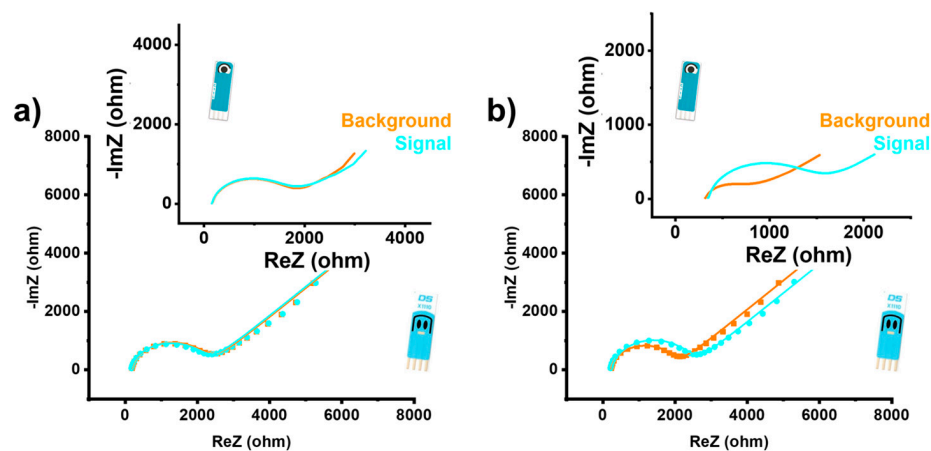

Figure 4. EIS (Nyquist plot) recorded at dual immunosensor for the negative (**a**) and positive (**b**) control, along with the corresponding measurements using conventional single SPCE.

3.5. Performance in the Real Clinical Sample

We investigated the functioning of the immunosensor in a 20-fold diluted real serum sample with the concentration of anti-SARS-CoV-2 IgGs of 106 μg mL^{-1}, according to ELISA assay. The impedimetric signals showed relatively low standard error (ΔR_{ct} = 2434.52 $\pm$ 88.92 ohms, n = 3), indicating very good stability of the sensor architecture even in the case of a real heterogeneous sample. On the basis of the standard calibration protocol, the value obtained corresponds to the anti-SARS-CoV-2 IgG concentration of 85 $\pm$ 18 μg mL^{-1}, which is in fairly good agreement with ELISA. The corresponding EIS (Nyquist plots) are presented in Figure 5. It should be mentioned that the RBD-based immunosensor detects both IgG and IgM antibodies, the latter being dominant in the early immune response.
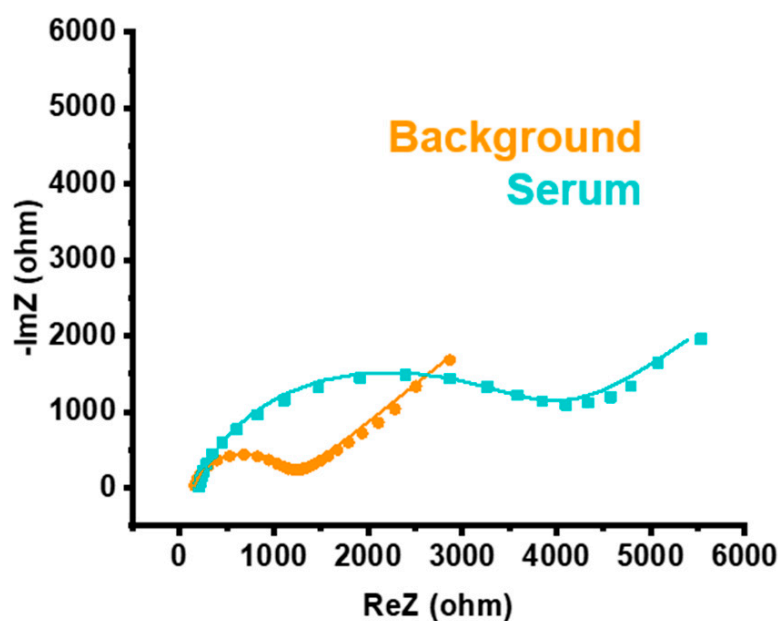

Figure 5. EIS (Nyquist plots) recorded with the immunosensor in a real serum of an infected person.

3.6. Amplification Mode

We also tested the immunosensor using the amplification mode. In this case, the immunosensor was first exposed to a 10 μL sample containing human anti-SARS-CoV-2

IgG antibodies for one hour and then to 10 μL of unlabeled secondary goat anti-human IgG antibodies for another hour, the latter at a necessarily high concentration of 25 μg mL^{-1}, to amplify the analytical signal.

As shown in Figure 6, the amplification mode resulted in an extended linear range, and an even lower detection limit of 0.93 pM was achieved. However, in this case, we identified some degree of non-specific binding of the secondary unlabeled goat anti-human IgG antibodies associated with the negative control unit.
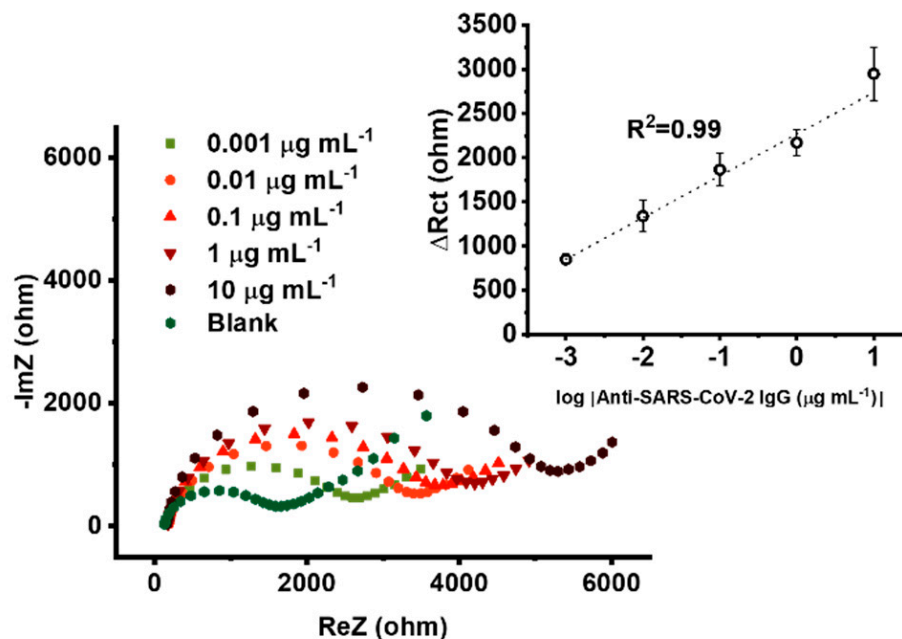

Figure 6. EIS (Nyquist plots) for different concentrations of anti-SARS-CoV-2 IgGs using amplification mode and the corresponding calibration plot (n = 4).

3.7. Comparison with Electrochemical Sensors for Anti-SARS-CoV-2 Antibodies

To the best of our knowledge, although a variety of electrochemical sensors for whole SARS-CoV-2 virus particles, spike proteins, and viral RNA exist [21,22], only a few comparable studies on electrochemical sensors for anti-SARS-CoV-2 antibodies have been published, namely by Rashed et al. [14], Bojórquez et al. [22], Torrente-Rodríguez et al. [37], Ali et al. [38], Jiang et al. [39], Liustrovaite et al. [40], Shoute et al. [41], and Yakoh et al. [42]. In addition to the differences in sensor architecture and analyte of interest, another key difference between the two classes of sensors is the matrix in which they are designed to operate. For virus sensors, this is nasopharyngeal fluid, whereas, for antibody sensors, it is usually blood plasma or serum. The main difference in the composition of the two fluids is the total protein content, which ranges from 0.1–2.2 mg mL^{-1} in nasopharyngeal fluid [43] and 60–80 mg mL^{-1} in plasma/serum [44].

A comparison of the characteristics of competing sensors with the sensor described in this work is shown in Table 1. It is important to note that two other studies [14,37] did not report parameters such as RSD or linear range, while the third study [38] used rabbit antibodies and serum, and therefore, their results cannot be directly extrapolated to human samples.

Table 1. Comparison of electrochemical immunosensors for anti-SARS-CoV-2 antibodies.

Sensing Principle	Substrate	Recognition Element	Target	Matrix	Integrated Negative Control	RSD	Limit of Detection (LOD)	Linear Range	Advantages	Disadvantages
Impedance spectroscopy [14]	Commercial electrochemical 16-well plate (ACEA Biosciences xCELLigence system)	SARS-CoV-2 RBD	Human anti-SARS-CoV-2 IgG antibodies	100× diluted human serum	Yes (1% milk solution)	Not reported	Not reported	Not reported	Label-free, Simple operation High sample, throughput, Negative control	High cost, Yes/no readout, Some key performance parameters not tested
Impedance spectroscopy [22]	Glass substrate with poly-dimethylsiloxane (PDMS) and Au nanowires	SARS-CoV-2 RBD	anti-SARS-CoV-2 IgG antibodies	100× diluted human plasma	No	Not reported as RSD	0.99 pg/mL	10^{-6}–10^{-16} g mL^{-1}	Label-free, Simultaneous detection of antigens and antibodies	Some key parameters not tested, Complex architecture
Amperometry (consumption of H$_2$O$_2$ by HRP-labeled secondary antibodies) [37]	Lab-made laser-engraved graphite electrodes	SARS-CoV-2 spike protein (S1)	Human anti-SARS-CoV-2 IgG and IgM antibodies	100× diluted human serum	No	8.4% for IgGs and 6.0% for IgMs	Not reported	1–500 ng mL^{-1} for both IgGs and IgMs	Simple operation, Multiplex, platform for several analytes (antigen, antibodies, C-reactive protein)	LOD not tested, Observed interference from SARS-CoV nucleocapsid protein
Impedance spectroscopy [38]	Aerosol jet nanoprinted reduced-graphene-oxide-coated 3D electrodes	SARS-CoV-2 spike protein (S1) and RBD	Rabbit anti-SARS-CoV-2 IgG antibodies	Rabbit serum and fetal bovine serum (dilution not reported)	No	± 6.01% (12.02% in total, author's note)	2.8×10^{-15} M (4.2×10^{-4} ng mL^{-1} *) with S1 and 16.9×10^{-15} M (2.5×10^{-3} ng mL^{-1} *) with RBD as the recognition element (estimated from noise)	Two ranges: 1×10^{-12} –100×10^{-12} M (0.15–15 ng mL^{-1} *) and 100×10^{-12} –20×10^{-9} M (15–1000 ng mL^{-1} *)	Label-free, Fast response, Recoverable (one device can be used for several samples)	Complex architecture, construction process and operation, High cost, Operation in human samples may be different, Limit of detection estimated from blank/noise
Cyclic voltammetry [39]	Au nanoparticles modified screen-printed carbon electrodes	SARS-CoV-2 spike protein (S1)	anti-SARS-CoV-2 IgG antibodies	PBS	No	Not reported	1.28 pg mL^{-1}	fg mL^{-1} to ng mL^{-1}	Label-free, Fast response, Broad-dynamic range, Low cost Simple operation	No selectivity study reported
Cyclic voltammetry and Impedance [40] Spectroscopy	Lab-fabricated Au electrodes on microscope slides	SARS-CoV-2 spike protein	anti-SARS-CoV-2 spike antibodies	PBS and serum	No	Not reported	0.38 μg mL^{-1} and 0.30 μg mL^{-1}	4.5–22.5 μg mL^{-1}	Label-free, Simple operation	Narrow operating range, No selectivity study reported, Large custom-made electrodes, Common self-assembled monolayer protocol (SAM)

Table 1. *Cont.*

Sensing Principle	Substrate	Recognition Element	Target	Matrix	Integrated Negative Control	RSD	Limit of Detection (LOD)	Linear Range	Advantages	Disadvantages
Impedance spectroscopy [41]	Lab-made gold interdigitated microelectrode array	Trimeric SARS-CoV-2 spike protein	Total anti-SARS-CoV-2 spike antibodies	Human serum	No	Not reported	0.4 BAU mL^{-1} (upper detection limit >100 BAU mL^{-1}) *BAU corresponds to binding antibody units	1–100 BAU mL^{-1}	Non-Faradaic mode of operation (capacitive sensing), Label-free	Complex fabrication procedure, Common self-assembled monolayer protocol (SAM)
Square-wave voltammetry (attenuation of a redox probe signal after antibody binding) [42]	Lab-made, paper-based screen-printed graphene electrodes	SARS-CoV-2 RBD	Human anti-SARS-CoV-2 IgG and IgM antibodies	Human serum (dilution not reported)	No	4.2% for IgGs and 3.3% for IgMs	0.96 ng mL^{-1} for IgGs and 0.14 ng mL^{-1} for IgMs (estimated from noise)	1–1000 ng mL^{-1} (logarithm scale) for both IgGs and IgMs	Simple operation, Multiplex platform for several analytes (antigen and antibodies), Low cost	Limit of detection estimated from blank/noise
Impedance spectroscopy [this study]	Commercial screen-printed carbon electrodes	SARS-CoV-2 RBD	Human anti-SARS-CoV-2 IgG antibodies Kd = 6.3 nM [45]	20× diluted human serum	Yes (BSA)	ca. 10% for 0.1 µg mL^{-1} data point	26 pM (3.9 ng mL^{-1}) and 0.9 pM (0.13 ng mL^{-1}) in amplification mode	0.01–10 µg mL^{-1} and 0.001–10 10 µg mL^{-1} in amplification mode	Label-free, Simple operation, Simple to prepare, Integrated negative control unit, Possible signal amplification	Some degree of non-specific binding when using the amplification protocol

* Our recalculation based on the typical molecular mass of rabbit IgG antibodies, e.g., 150 kD (150,000 g mol^{-1}).

4. Conclusions

We demonstrated a simple, label-free, and sensitive immunosensor for impedimetric detection of human anti-SARS-CoV-2 IgGs. The sensing strategy involved cyclic voltammetric deposition of a polyaniline film on a screen-printed carbon electrode, followed by modification with glutaraldehyde and the RBD subunit of the SARS-CoV-2 spike glycoprotein and deposition of glycine to prevent non-specific binding. The immunosensor showed excellent sensitivity for the detection of SARS-CoV-2 infection in human serum. Practical applicability was addressed through a dual-working electrode configuration with an integrated negative control unit and by coupling the immunosensor to a portable potentiostat. The performance of the immunosensor was successfully tested by measuring human anti-SARS-CoV-2 IgGs in a real serum from an infected patient, achieving good agreement with a complementary ELISA assay. Such an immunosensor provides a promising and portable sensing platform for a simple immunoassay that meets the needs of both clinical diagnostics and vaccine efficacy monitoring. Additional signal amplification with secondary antibodies has been proposed, but some degree of non-specific binding at the negative control unit has been observed within this operation mode. It is worth mentioning that matrix variations should be taken into account in such immunosensing. Improved sensor-to-sensor reproducibility could be achieved by introducing chemical and/or electrochemical pretreatment protocols for commercial supporting screen-printed electrodes.

References

1. Johns Hopkins. University of Medicine, Coronavirus Resource Center. Available online: https://coronavirus.jhu.edu/map.html (accessed on 7 March 2023).
2. Nishiga, M.; Wang, D.W.; Han, Y.; Lewis, D.B.; Wu, J.C. COVID-19 and cardiovascular disease: From basic mechanisms to clinical perspectives. *Nat. Rev. Cardiol.* **2020**, *17*, 543–558. [CrossRef] [PubMed]
3. Corman, V.M.; Landt, O.; Kaiser, M.; Molenkamp, R.; Meijer, A.; Chu, D.K.; Bleicker, T.; Brünink, S.; Schneider, J.; Schmidt, M.L.; et al. Detection of 2019 novel coronavirus (2019-nCoV) by real-time RT-PCR. *Eurosurveillance* **2020**, *25*, 2000045. [CrossRef] [PubMed]

4. Van Elden, L.J.R.; van Loon, A.M.; van Alphen, F.; Hendriksen, K.A.W.; Hoepelman, A.I.M.; van Kraaiji, M.G.J.; Oosterheert, J.-J.; Schipper, P.; Schuurman, R.; Nijhuis, M. Frequent detection of human coronaviruses in clinical specimens from patients with respiratory tract infection by use of a novel real-time reverse transcriptase polymerase chain reaction. *J. Infect. Dis.* **2004**, *189*, 652–657. [CrossRef]

5. Gootenberg, J.S.; Abudayyeh, O.O.; Lee, J.W.; Essletzbichler, P.; Dy, A.J.; Joung, J.; Verdine, V.; Donghia, N.; Daringer, N.M.; Freije, C.A.; et al. Nucleic acid detection with CRISPR-Cas13a/C2c2. *Science* **2017**, *356*, 438–442. [CrossRef] [PubMed]

6. Pang, B.; Xu, J.; Liu, Y.; Peng, H.; Feng, W.; Cao, Y.; Wu, J.; Xiao, H.; Pabbaraju, K.; Tipples, G.; et al. Isothermal amplification and ambient visualization in a single tube for the detection of SARS-CoV-2 using loop-mediated amplification and CRISPR technology. *Anal. Chem.* **2020**, *92*, 16204–16212. [CrossRef] [PubMed]

7. Wang, R.; Qian, C.; Pang, Y.; Li, M.; Yang, Y.; Ma, H.; Zhao, M.; Qian, F.; Yu, H.; Liu, Z.; et al. opvCRISPR: One-pot visual RT-LAMP-CRISPR platform for SARS-cov-2 detection. *Biosen. Bioelectron.* **2020**, *172*, 112766. [CrossRef]

8. Chen, Z.; Zhang, Z.; Zhai, X.; Li, Y.; Lin, L.; Zhao, H.; Bian, L.; Li, P.; Yu, L.; Wu, Y.; et al. Rapid and sensitive detection of anti-SARS-CoV-2 IgG, using lanthanide-doped nanoparticles-based lateral flow immunoassay. *Anal. Chem.* **2020**, *92*, 7226–7231. [CrossRef] [PubMed]

9. MacMullan, M.A.; Ibrayeva, A.; Trettner, K.; Deming, L.; Das, S.; Tran, F.; Moreno, J.R.; Casian, J.G.; Chellamuthu, P.; Kraft, J.; et al. ELISA detection of SARS-CoV-2 antibodies in saliva. *Sci. Rep.* **2020**, *10*, 20818. [CrossRef] [PubMed]

10. Mattioli, I.A.; Hassan, A.; Oliveira, O.N., Jr.; Crespilho, F.N. On the challenges for the diagnosis of SARS-CoV-2 based on a review of current methodologies. *ACS Sens.* **2020**, *5*, 3655–3677. [CrossRef] [PubMed]

11. Zhang, X.; Liu, W.; Lu, X.; Gooding, J.J.; Li, Q.; Qu, K. Monitoring the progression of loop-mediated isothermal amplification using conductivity. *Anal. Biochem.* **2014**, *466*, 16–18. [CrossRef] [PubMed]

12. Chaibun, T.; Puenpa, J.; Ngamdee, T.; Boonapatcharoen, N.; Athamanolap, P.; O'Mullane, A.P.; Vongpunsawad, S.; Poovorawan, Y.; Lee, S.Y.; Lertanantawong, B. Rapid electrochemical detection of coronavirus SARS-CoV-2. *Nat. Comm.* **2021**, *12*, 802. [CrossRef] [PubMed]

13. Fabiani, L.; Saroglia, M.; Galatà, G.; De Santis, R.; Fillo, S.; Luca, V.; Faggioni, G.; D'Amore, N.; Regalbuto, E.; Salvatori, P.; et al. Magnetic beads combined with carbon black-based screen-printed electrodes for COVID-19: A reliable and miniaturized electrochemical immunosensor for SARS-CoV-2 detection in saliva. *Biosen. Bioelectron.* **2021**, *171*, 112686. [CrossRef] [PubMed]

14. Rashed, M.Z.; Kopechek, J.A.; Priddy, M.C.; Hamorsky, K.T.; Palmer, K.E.; Mittal, N.; Valdez, J.; Flynn, J.; Williams, S.J. Rapid detection of SARS-CoV-2 antibodies using electrochemical impedance-based detector. *Biosen. Bioelectron.* **2021**, *171*, 112709. [CrossRef]

15. Vadlamani, B.S.; Uppal, T.; Verma, S.C.; Misra, M. Functionalized TiO_2 nanotube-based electrochemical biosensor for rapid detection of SARS-CoV-2. *Sensors* **2020**, *20*, 5871. [CrossRef] [PubMed]

16. Yousefi, H.; Mahmud, A.; Chang, D.; Das, J.; Gomis, S.; Chen, J.B.; Wang, H.; Been, T.; Yip, L.; Coomes, E.; et al. Detection of SARS-CoV-2 viral particles using direct, reagent-free electrochemical sensing. *J. Am. Chem. Soc.* **2021**, *143*, 1722–1727. [CrossRef] [PubMed]

17. Zhao, H.; Liu, F.; Xie, W.; Zhou, T.C.; OuYang, J.; Jin, L.; Li, H.; Zhao, C.Y.; Zhang, L.; Wei, J.; et al. Ultrasensitive supersandwich-type electrochemical sensor for SARS-CoV-2 from the infected COVID-19 patients using a smartphone. *Sens. Actuators B Chem.* **2021**, *327*, 128899. [CrossRef]

18. Jaewjaroenwattana, J.; Phoolcharoen, W.; Pasomsub, E.; Teengam, P.; Chailapakul, O. Electrochemical paper-based antigen sensing platform using plant-derived monoclonal antibody for detecting SARS-CoV-2. *Talanta* **2023**, *251*, 123783. [CrossRef] [PubMed]

19. Adeel, M.; Asif, K.; Alshabouna, F.; Canzonieri, V.; Rahman, M.M.; Ansari, S.A.; Guder, F.; Rizzolio, F.; Daniele, S. Label-free electrochemical aptasensor for the detection of SARS-CoV-2 spike protein based on carbon cloth sputtered gold nanoparticles. *Biosens. Bioelectron. X* **2022**, *12*, 100256. [CrossRef] [PubMed]

20. Mavrikou, S.; Moschopoulou, G.; Tsekouras, V.; Kintzios, S. Development of a portable, ultra-rapid and ultra-sensitive cell-based biosensor for the direct detection of the SARS-CoV-2 S1 spike protein antigen. *Sensors* **2020**, *20*, 3121. [CrossRef]

21. Cancino-Bernardi, J.; Comparetti, E.J.; Ferreira, N.N.; Miranda, R.R.; Tuesta, M.M.; Sampaio, I.; da Costa, P.I.; Zucolotto, V. A SARS-CoV-2 impedimetric biosensor based on the immobilization of ACE-2 receptor-containing entire cell membranes as the biorecognition element. *Talanta* **2023**, *253*, 124008. [CrossRef]

22. Sandoval Bojórquez, D.I.; Janićijević, Z.; Palestina Romero, B.; Oliveros Mata, E.S.; Laube, M.; Feldmann, A.; Kegler, A.; Drewitz, L.; Fowley, C.; Pietzsch, J.; et al. Impedimetric Nanobiosensor for the Detection of SARS-CoV-2 Antigens and Antibodies. *ACS Sens.* **2023**, *8*, 576–586. [CrossRef] [PubMed]

23. Seo, G.; Lee, G.; Kim, M.J.; Baek, S.H.; Choi, M.; Ku, K.B.; Lee, C.-S.; Jun, S.; Park, D.; Kim, H.G.; et al. Rapid detection of COVID-19 causative virus (SARS-CoV-2) in human nasopharyngeal swab specimens using field-effect transistor-based biosensor. *ACS Nano* **2020**, *14*, 5135–5142. [CrossRef]

24. Raziq, A.; Kidakova, A.; Boroznjak, R.; Reut, J.; Öpik, A.; Syritski, V. Development of a portable MIP-based electrochemical sensor for detection of SARS-CoV-2 antigen. *Biosens. Bioelectron.* **2021**, *178*, 113029. [CrossRef] [PubMed]

25. Ranjan, P.; Singhal, A.; Yadav, S.; Kumar, N.; Murali, S.; Sanghi, S.K.; Khan, R. Rapid diagnosis of SARS-CoV-2 using potential point-of-care electrochemical immunosensor: Toward the future prospects. *Int. Rev. Immunol.* **2021**, *40*, 126–142. [CrossRef] [PubMed]

26. Mahshid, S.S.; Flynn, S.E.; Mahshid, S. The potential application of electrochemical biosensors in the COVID-19 pandemic: A perspective on the rapid diagnostics of SARS-CoV-2. *Biosen. Bioelectron.* **2021**, *176*, 112905. [CrossRef] [PubMed]

27. AAT Bioquest. Buffer Preparations and Recipes. Available online: https://www.aatbio.com/resources/buffer-preparations-and-recipes/ (accessed on 14 May 2020).

28. Dhand, C.; Das, M.; Datta, M.; Malhotra, B.D. Recent advances in polyaniline based biosensors. *Biosen. Bioelectron.* **2011**, *26*, 2811–2821. [CrossRef] [PubMed]

29. Cai, Q.; Xu, B.; Ye, L.; Di, Z.; Zhang, J.; Jin, Q.; Zhao, J.; Xue, J.; Chen, X. Immobilization of biomolecules on cysteamine-modified polyaniline film for highly sensitive biosensing. *Talanta* **2014**, *120*, 462–469. [CrossRef]

30. Sai, V.V.R.; Mahajan, S.; Contractor, A.Q.; Mukherji, S. Immobilization of antibodies on polyaniline films and its application in a piezoelectric immunosensor. *Anal. Chem.* **2006**, *78*, 8368–8373. [CrossRef]

31. De Melo, J.V.; Bello, M.E.; De Azevedo, W.M.; De Souza, J.M.; Diniz, F.B. The effect of glutaraldehyde on the electrochemical behavior of polyaniline. *Electrochim. Acta* **1999**, *44*, 2405–2412. [CrossRef]

32. Grothe, R.A.; Lobato, A.; Mounssef, B.; Tasić, N.; Braga, A.A.; Maldaner, A.O.; Maldaner, A.O.; Aldous, L.; Paixão, T.R.L.C.; Gonçalves, L.M. Electroanalytical profiling of cocaine samples by means of an electropolymerized molecularly imprinted polymer using benzocaine as the template molecule. *Analyst* **2021**, *146*, 1747–1759. [CrossRef] [PubMed]

33. Jeon, J.W.; Kwon, S.R.; Lutkenhaus, J.L. Polyaniline nanofiber/electrochemically reduced graphene oxide layer-by-layer electrodes for electrochemical energy storage. *J. Mater. Chem. A* **2015**, *7*, 3757. [CrossRef]

34. Coetzee, J.; Van der Merwe, C.F. Some characteristics of the buffer vehicle in glutaraldehyde-based fixatives. *J. Microsc.* **1987**, *146*, 143–155. [CrossRef]

35. Luisetto, M.; Tarro, G.; Edbey, K.; Khan, F.A.; Yesvi, A.R.; Nili, B.A.; Fiazza, C.; Mashori, G.R.; Latyshev, O.V. Coronavirus COVID-19 surface properties: Electrical charges status. *Int. J.* **2021**, *2766*, 3264. [CrossRef]

36. Al Sarkhi, A.K. Hypothesis: The electrical properties of coronavirus. *Electromagn. Biol. Med.* **2020**, *39*, 433–436. [CrossRef]

37. Torrente-Rodríguez, R.M.; Lukas, H.; Tu, J.; Min, J.; Yang, Y.; Xu, C.; Rossiter, H.B.; Gao, W. SARS-CoV-2 RapidPlex: A Graphene-Based Multiplexed Telemedicine Platform for Rapid and Low-Cost COVID-19 Diagnosis and Monitoring. *Matter* **2020**, *3*, 1981–1998. [CrossRef] [PubMed]

38. Ali, M.A.; Hu, C.; Jahan, S.; Yuan, B.; Saleh, M.S.; Ju, E.; Gao, S.-J.; Panat, R. Sensing of COVID-19 Antibodies in Seconds via Aerosol Jet Nanoprinted Reduced-Graphene-Oxide-Coated 3D Electrodes. *Adv. Mater.* **2021**, *33*, 2006647. [CrossRef] [PubMed]

39. Jiang, F.; Xiao, Z.; Wang, T.; Wang, J.; Bie, L.; Saleh, L.; Frey, K.; Zhang, L.; Wang, J. Rapid and sensitive multiplex detection of COVID-19 antigens and antibody using electrochemical immunosensor-/aptasensor-enabled biochips. *Chem. Commun.* **2022**, *58*, 7285–7288. [CrossRef] [PubMed]

40. Liustrovaite, V.; Drobysh, M.; Rucinskiene, A.; Baradoke, A.; Ramanaviciene, A.; Plikusiene, I.; Samukaite-Bubniene, U.; Viter, R.; Chen, C.-F.; Ramanavicius, A. Towards an electrochemical immunosensor for the detection of antibodies against SARS-CoV-2 spike protein. *J. Electrochem. Soc.* **2022**, *169*, 037523. [CrossRef]

41. Shoute, L.C.; Abdelrasoul, G.N.; Ma, Y.; Duarte, P.A.; Edwards, C.; Zhuo, R.; Zeng, J.; Feng, Y.; Charlton, C.L.; Kanji, J.N.; et al. Label-free impedimetric immunosensor for point-of-care detection of COVID-19 antibodies. *Microsyst. Nanoeng.* **2023**, *9*, 3. [CrossRef]

42. Yakoh, A.; Pimpitak, U.; Rengpipat, S.; Hirankarn, N.; Chailapakul, O.; Chaiyo, S. Paper-based electrochemical biosensor for diagnosing COVID-19: Detection of SARS-CoV-2 antibodies and antigen. *Biosens. Bioelectron.* **2021**, *176*, 112912. [CrossRef] [PubMed]

43. Rossen, R.D.; Schade, A.L.; Butler, W.T.; Kasel, J.A. The proteins in nasal secretion: A longitudinal study of the gammaA-globulin, gammaG-globulin, albumin, siderophilin, and total protein concentrations in nasal washings from adult male volunteers. *J. Clin. Investig.* **1966**, *45*, 768–776. [CrossRef] [PubMed]

44. Leeman, M.; Choi, J.; Hansson, S.; Storm, M.U.; Nilsson, L. Proteins and antibodies in serum, plasma, and whole blood—Size characterization using asymmetrical flow field-flow fractionation (AF4). *Anal. Bioanal. Chem.* **2018**, *410*, 4867–4873. [CrossRef] [PubMed]

45. Tian, X.; Li, C.; Huang, A.; Xia, S.; Lu, S.; Shi, Z.; Lu, L.; Jiang, S.; Yang, Z.; Wu, Y.; et al. Potent binding of 2019 novel coronavirus spike protein by a SARS coronavirus-specific human monoclonal antibody. *Emerg. Microbes Infect.* **2020**, *9*, 382–385. [CrossRef] [PubMed]